Available online at www.sciencedirect.com
SCIENCE DIRECT®
International Journal of Heat and Fluid Flow 26 (2005) 378–392
International Journal of HEAT AND FLUID FLOW
www.elsevier.com/locate/ijhff

Large eddy simulation of turbulent flows in a rotating concentric annular channel

Nan-Sheng Liu, Xi-Yun Lu *

Department of Modern Mechanics, University of Science and Technology of China, Hefei, Anhui 230026, PR China

Received 19 January 2004; accepted 27 October 2004
Available online 19 December 2004

Abstract

Turbulent flow through a concentric annular channel rotating around its axis is investigated numerically by use of large eddy simulation (LES) coupled with a localized one-equation dynamic subgrid-scale (SGS) model (LDM). The objective of this study is to investigate the behavior of turbulent flow near the inner and outer walls of the rotating concentric annular channel and to examine the effectiveness of the LES technique for predicting the turbulent flow subjected to system rotation. The Reynolds number, based on the global friction velocity u_τ and the annular channel gap width d, is 640, and the rotation number $N = 0$–20, which is defined as $N = 2\Omega d/u_\tau$ with Ω being the angular velocity of the rotating annular channel. To validate the present computation, LES on turbulent flows in a rotating pipe and in a concentric annular channel are carried out, which shows that the LES results are in good agreement with available experimental data and direct numerical simulation (DNS) results. Then, turbulent statistics in the rotating annular channel, including the resolved velocity, turbulence intensities, Reynolds stresses, turbulence skewness and flatness, and flow structures near the walls, are investigated. The budgets of turbulent kinetic energy and Reynolds stresses are calculated to examine the turbulence production rate, velocity and pressure-gradient correlation, turbulence diffusion, dissipation rate and Coriolis force term near the outer and inner walls.

Keywords: Large eddy simulation (LES); Subgrid-scale (SGS) model; Localized dynamic SGS model; Turbulent annular channel flow; Rotating turbulent flow

1. Introduction

Rotating turbulent flows have been studied extensively because of its wide application in engineering, such as those in gas turbine blade passages, nuclear reactor cores, combustion systems, and rotating heat exchangers. In these flows, the rotation induces additional body forces, i.e., centrifugal and Coriolis forces, acting on the turbulent structures, so that the momentum transfer mechanism becomes more complex. Thus, the fundamental mechanism and main statistical characteristics of the turbulent flow near the walls need to be investigated in detail. Usually, turbulent flow through a concentric annular channel rotating around its axis is a typical case among the rotating turbulent flows. The distinctive feature of turbulent flow in the concentric annular channel is that the velocity field is asymmetric about the central line of annular channel. The asymmetric velocity field results from the fact that the local Reynolds numbers, which are defined based on the inner and outer cylinder radii respectively, are different near the inner and outer wall regions. It is expected that the turbulent transport phenomena in such flows differ from those in the symmetrical flows, such as the plane channel flow. Even though the turbulent flow subjected to system rotation has attracted considerable

* Corresponding author. Tel.: +86 551 360 3223; fax: +86 551 360 6459.
E-mail address: xlu@ustc.edu.cn (X.-Y. Lu).

0142-727X/$ - see front matter © 2004 Elsevier Inc. All rights reserved.
doi:10.1016/j.ijheatfluidflow.2004.10.005

interest since the Coriolis force plays an important role to change the turbulence features, the asymmetric flow in an axially rotating annular channel, which is speculated to be different from the turbulent flow in a rotating plane channel, still catches little attention. In the following, the relevant work on the turbulent annular channel flow and rotating turbulent flow is briefly reviewed.

Some experiments on turbulent annular channel flow have been performed. Brighton (1963) and Brighton and Jones (1964) measured the turbulence intensities and shear stresses. Rehme (1975) investigated the turbulence in the concentric annuli with different small radius ratios, defined as the inner cylinder radius to the outer cylinder radius. Nouri et al. (1993) and Escudier et al. (1995) performed experiments to observe the flow characteristics of Newtonian and non-Newtonian fluids in an annular channel. Meanwhile, some experiments on the annular channel flow involved heat transfer have been carried out. Heikal et al. (1976) measured the velocity field of heated airflow through an annular channel. Hasan et al. (1992), Velidandla et al. (1996) and Kang et al. (2001) took experimental studies on the velocity and temperature fields of the unheated and heated turbulent liquid flow through a vertical concentric annular channel.

On the other hand, numerical computations have been performed on the turbulent flow in concentric annular channel. Hanjalic (1974) studied turbulence features in annular ducts based on the Reynolds-averaged Navier–Stokes equations (RANS) with a differential transport model. Malik and Pletcher (1981) examined the performance of some typical turbulence models on the flow with heat transfer in the ducts. Azouz and Shirazi (1998) used RANS technique to calculate the turbulent flow in concentric annuli, and compared their results with the experimental data given by Nouri et al. (1993). Zarate et al. (2001) carried out numerical simulation with RANS method on the isothermal and heated turbulent upflow in a vertical concentric annular channel, with its inner wall heated. Recently, Chung et al. (2002) performed a direct numerical simulation (DNS) on turbulent annular channel flow at low Reynolds number.

Turbulent flows in rotating reference frames are of considerable importance in applications and fundamentals. It is well known that system rotation can change the near-wall turbulent burst events to modify the mean velocity, turbulence intensity and Reynolds stresses. Johnston et al. (1972) observed the rotation-induced alteration of turbulence level in a spanwise rotating channel, augmented in the destabilized wall region while suppressed in the stabilized wall region. Tritton (1992) proposed a 'simplified Reynolds stress equation scheme' (i.e., SRSE scheme) to clarify and synthesize some typical concepts underlying stabilization, destabilization and re-stabilization, and the role of shear/Coriolis instability occurring in rotating fluid. Kristoffersen and Andersson (1993) reported the rotation-induced large-scale disturbances in their DNS on the spanwise rotating channel flow, which are the Taylor–Görtler-like vortical structures near the destabilized wall. Based on their DNS on the rotating pipe flow, Orlandi and Fatica (1997) claimed that system rotation modifies the size of the near-wall vortical structures and their tilting to the wall, which makes the turbulence in the wall region more intermittent. Speziale et al. (2000) paid particular attention to the closure of rotating turbulence in an axially rotating pipe. El-Samni and Kasagi (2001) investigated the effects of system rotation with three orthogonal rotating axes on the turbulent channel flow based on their DNS. Recently, Wu and Kasagi (2004) dealt with the effects of arbitrary directional system rotation on turbulent channel flow in detail.

Usually, large eddy simulation (LES) technique provides an effective tool for the prediction of complex turbulent flows by computing only the large-scale motion and modeling the subgrid-scale (SGS) motion. The accuracy of the LES method depends significantly on the ability of the SGS model to characterize the interaction between the resolved and unresolved motions. The performance of the classical algebraic eddy-viscosity model proposed by Smagorinsky (1963) showed that this model is accurate only as long as the inertial range is resolved, and even then the model coefficient had to be varied for different flows, which makes the universal application of this model questionable. Germano et al. (1991) developed a dynamic approach whereby the model coefficient is computed as a part of the solution itself, which resulted in a major advancement in the subgrid stress modeling. To reasonably model the SGS stress in rotating turbulence, a subgrid-scale stress model named by localized one-equation dynamic model (LDM) is adopted to closure the filtered Navier–Stokes equations. The LDM is proposed by Kim and Menon (1997), who used the similarity between the subgrid-scale stress tensor and the test-scale Leonard stress tensor, found experimentally by Liu et al. (1994), to evaluate the dynamic model coefficients. The LDM was proved to be capable to predict complicated turbulent wall shear flows (Kim and Menon, 1999) and turbulent flow in a rotating duct (Pallares and Davidson, 2000).

Here, the LDM is employed to investigate the turbulent flow in an annular channel rotating about its axis. To the best of our knowledge, however, turbulent flows in a rotating concentric annular channel have never been studied by means of LES method. To validate our computational code, the LES coupled with the LDM are performed on the turbulent flows in a rotating pipe and a concentric annular channel. It is shown that the LES results are compared well with DNS results (Orlandi and Fatica, 1997) and experimental data (Reich and Beer, 1989; Nouri et al., 1993). The motivation of this study is to deal with the behaviors of turbu-

lent flow near the inner and outer walls of the rotating concentric annular channel and to examine the effectiveness of the LES technique for predicting the turbulent flow influenced by system rotation.

This paper is organized as follows. The governing equations and the localized one-equation dynamic SGS model are described in the next section. In Section 3, the numerical method and its validation are presented. In Section 4, LES results of the rotating annular channel flow, including the mean velocity, turbulence intensities and Reynolds stresses, flatness and skewness of the velocity fluctuations, turbulence budgets of the turbulent kinetic energy, and flow structures, are shown and discussed. Conclusions are summarized in Section 5.

2. Governing equations

2.1. Filtered Navier–Stokes equations

In LES approach, by applying a filtering operation, all the flow variables are decomposed into resolved large-scale components (denoted by an overbar) and unresolved SGS components, and the three-dimensional resolved Navier–Stokes equations are used as the governing equations. To non-dimensionalize the governing equations, as shown in Fig. 1, the gap width of the annular channel, $d = R_o - R_i$, is used as the length scale, where R_o and R_i are the outer and inner cylinder radii respectively, and the global friction velocity u_τ as the velocity scale, which is described in the following. Then, the non-dimensional governing equations in rotating frame are given as

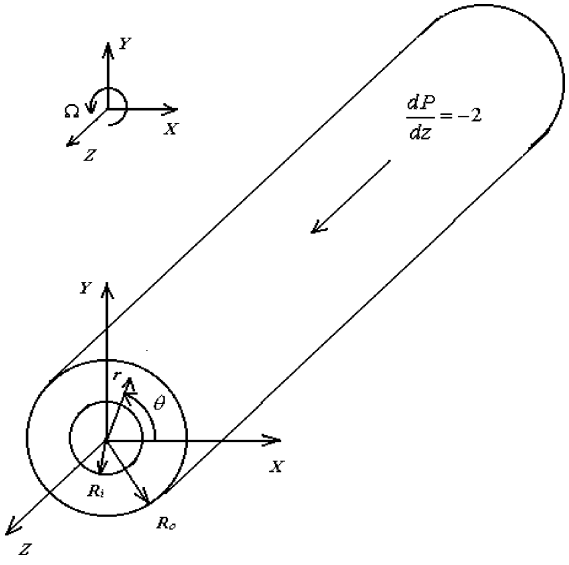

Fig. 1. Sketch of the concentric annular channel.

$$\frac{\partial \bar{u}_i}{\partial x_i} = 0 \tag{1}$$

$$\frac{\partial \bar{u}_i}{\partial t} + \frac{\partial (\bar{u}_i \bar{u}_j)}{\partial x_j} = -\frac{\partial \bar{p}}{\partial x_i} + \frac{1}{Re_\tau}\frac{\partial^2 \bar{u}_i}{\partial x_j \partial x_j} - N\varepsilon_{ijk}\frac{\Omega_j}{\Omega}\bar{u}_k - \frac{\partial \tau_{ij}}{\partial x_j} \tag{2}$$

where Re_τ is the Reynolds number, defined as $Re_\tau = u_\tau d/\nu$ with ν being the kinematic viscosity of the fluid, N represents the rotation number $N = 2\Omega d/u_\tau$ with Ω being the angular velocity of the axially rotating annular channel. τ_{ij} is the SGS stress tensor,

$$\tau_{ij} = \overline{u_i u_j} - \bar{u}_i \bar{u}_j \tag{3}$$

The annular channel flow is driven by an imposed non-dimensional mean pressure gradient $\overline{\mathrm{d}P}/\mathrm{d}z = -2$ along the axial direction. As fully developed turbulent flow is assumed here, the global velocity u_τ is defined as

$$u_\tau = \left(-\frac{d}{2\rho}\frac{\overline{\mathrm{d}P}^*}{\mathrm{d}z^*}\right)^{1/2} \tag{4}$$

where ρ is the fluid density and $\overline{\mathrm{d}P}^*/\mathrm{d}z^*$ identifies the dimensional mean pressure gradient.

It is a natural choice to solve the filtered Navier–Stokes equations in cylindrical coordinates. Following the approach proposed by Verzicco and Orlandi (1996), new variables $q_r = r\bar{v}_r$, $q_\theta = r\bar{v}_\theta$, and $q_z = \bar{v}_z$ are introduced, where $\bar{v}_r$, $\bar{v}_\theta$ and $\bar{v}_z$ represent the resolved radial, azimuthal and axial velocity components, respectively. The governing equations in terms of the new variables are employed and solved numerically in this study.

Since the turbulent flow in the annular channel is assumed to be fully developed, periodic boundary condition is used in the axial direction. No-slip and no-penetration velocity boundary conditions are set on the inner and outer walls. The solution of laminar annular channel flow with imposed random disturbances is used as an initial flow field.

2.2. Localized one-equation dynamic subgrid-scale model

In the localized dynamic model, the grid size is used to characterize the length scale and the velocity scale is obtained by the SGS kinetic energy

$$k_{\mathrm{SGS}} = \frac{1}{2}(\overline{u_k u_k} - \bar{u}_k \bar{u}_k) \tag{5}$$

Here, k_{SGS} can be determined by solving the transport equation for the SGS kinetic energy (Schumann, 1975; Menon et al., 1996)

$$\frac{\partial k_{\mathrm{SGS}}}{\partial t} + \frac{\partial k_{\mathrm{SGS}}\bar{u}_j}{\partial x_j} = -\tau_{ij}\frac{\partial \bar{u}_i}{\partial x_j} - \varepsilon_{\mathrm{SGS}} + \frac{\partial}{\partial x_j}\left(\nu_\tau \frac{\partial k_{\mathrm{SGS}}}{\partial x_j}\right) \tag{6}$$

where the terms on the right-hand-side represent the production, dissipation and diffusion of k_{SGS}, respec-

tively, and v_τ denotes the eddy viscosity. Then, the SGS stress tensor τ_{ij} is represented as (Yoshizawa and Horiuti, 1985; Piomelli, 1993)

$$\tau_{ij} = -2v_\tau \bar{s}_{ij} + \frac{2}{3}\delta_{ij}k_{\mathrm{SGS}} \tag{7}$$

$$v_\tau = C_\tau \bar{\Delta} k_{\mathrm{SGS}}^{1/2} \tag{8}$$

where C_τ is an adjustable coefficient to be determined dynamically, $\bar{\Delta}$ is the grid filter width, and $\bar{s}_{ij}$ is the resolved-scale strain rate tensor

$$\bar{s}_{ij} = \frac{1}{2}(\bar{u}_{i,j} + \bar{u}_{j,i}) \tag{9}$$

Eq. (6) is closed once the SGS dissipation rate $\varepsilon_{\mathrm{SGS}}$ is modeled. Based on the scale analysis (Yoshizawa and Horiuti, 1985; Piomelli, 1993), $\varepsilon_{\mathrm{SGS}}$ is usually modeled as

$$\varepsilon_{\mathrm{SGS}} = C_\varepsilon \frac{k_{\mathrm{SGS}}^{3/2}}{\bar{\Delta}} \tag{10}$$

where C_ε is another coefficient which is also needed to be determined dynamically.

To obtain the coefficients in the LDM, the procedure to dynamically compute the model coefficients, i.e., C_τ and C_ε, is taken by introducing the definition of a test scale filter. The discretization form of the test filtering operation is the same as that proposed by Zang et al. (1993). Based on experimental finding (Liu et al., 1994), the similarity between the dynamic Leonard stresses, $L_{ij} = \bar{u}_i\bar{u}_j - \hat{\bar{u}}_i\hat{\bar{u}}_j$, and the SGS stresses allows reasonable assumption of the similar formulation for tensors τ_{ij} and L_{ij},

$$L_{ij} = -2C_\tau \hat{\Delta} k_{\mathrm{test}}^{1/2}\hat{\bar{s}}_{ij} + \frac{1}{3}\delta_{ij}L_{kk} \tag{11}$$

where k_{test} is the resolved kinetic energy at the test scale and is given as

$$k_{\mathrm{test}} = \frac{1}{2}(\bar{u}_k\bar{u}_k - \hat{\bar{u}}_k\hat{\bar{u}}_k) \tag{12}$$

Here, note that $k_{\mathrm{test}} = L_{kk}/2$. The energy is produced at the large scales by $-L_{ij}(\partial\hat{\bar{u}}_i/\partial x_j)$ and is dissipated by

$$e = (v + v_\tau)\left(\widehat{\frac{\partial\bar{u}_i}{\partial x_j}\frac{\partial\bar{u}_i}{\partial x_j}} + \frac{\partial\hat{\bar{u}}_i}{\partial x_j}\frac{\partial\hat{\bar{u}}_i}{\partial x_j}\right) \tag{13}$$

The dynamic model coefficient C_τ in Eq. (11) can be determined by the resolved quantities at the test filter level based on the least-square method suggested by Lilly (1992),

$$C_\tau = \frac{1}{2}\frac{L_{ij}\sigma_{ij}}{\sigma_{ij}\sigma_{ij}} \tag{14}$$

and

$$\sigma_{ij} = -\hat{\Delta} k_{\mathrm{test}}^{1/2}\hat{\bar{s}}_{ij} \tag{15}$$

It should be noted that σ_{ij} is determined completely by the quantities at the test filter level.

Similarity between the dissipation rates $\varepsilon_{\mathrm{SGS}}$ at the grid filter level and e at the test filter level is also applied to obtain the dissipation model coefficient in the model, i.e.,

$$e = C_\varepsilon \frac{k_{\mathrm{test}}^{3/2}}{\hat{\Delta}} \tag{16}$$

Then C_ε can be solved by Eq. (13) and written as

$$C_\varepsilon = \hat{\Delta}(v + v_\tau)\left(\widehat{\frac{\partial\bar{u}_i}{\partial x_j}\frac{\partial\bar{u}_i}{\partial x_j}} - \frac{\partial\hat{\bar{u}}_i}{\partial x_j}\frac{\partial\hat{\bar{u}}_i}{\partial x_j}\right)\Big/ k_{\mathrm{test}}^{3/2} \tag{17}$$

It can be verified that the LDM is a Galilean-invariant model and satisfies the realizability conditions proposed by Schumann (1977). Furthermore, k_{SGS} provides an accurate estimation for the SGS velocity scale with respect to the eddy viscosity model (Germano et al., 1991). The additional computational cost is primarily due to the inclusion of a transport equation for k_{SGS}, but the cost of the dynamic procedure is nearly the same as that of Germano-type dynamic model.

3. Numerical method and validation

3.1. Numerical method

In the present LES, the three sub-step fractional finite different method is employed to solve the governing equations. All the spatial derivatives are discretized by second-order central difference scheme; the convection and viscous terms are treated by Adams–Bashforth and Crank–Nicholson schemes, respectively. A third order Runge-Kutta scheme is used for time advancement. The low-storage Runge-Kutta method has an additional advantage that the minimum amount of computer run-time memory is required. Detailed description of the numerical method has been given by Rai and Moin (1991) and Verzicco and Orlandi (1996).

3.2. Validation

To validate the performance of the computational code, the LES with the LDM are carried out on the turbulent flows in a rotating pipe and in a concentric annular channel to compare the LES results with the available experimental data and DNS results.

In the LES of turbulent flows in a rotating pipe, the Reynolds number, defined as $Re_{\mathrm{m}} = U_{\mathrm{b}}R/v$, is 4900,

and the rotation number, $N = 2\Omega R/U_b$, is chosen as 0, 1 and 2, where U_b denotes the bulk mean velocity, Ω the angular velocity and R the pipe radius. The grid number $65 \times 65 \times 97$ in the radial, azimuthal and axial directions, respectively, is used. Meanwhile, to evaluate the performance of the LDM on the prediction of rotating turbulent flow, the LES coupled with dynamic Smagorinsky model (DSM) proposed by Germano et al. (1991) is also performed at $N = 1$.

Fig. 2(a) and (b) shows the profiles of the mean axial velocity normalized by the bulk mean velocity U_b and the azimuthal velocity normalized by the pipe wall rotating speed, respectively, where $r_d = (R - r)/R$. The LES results are in good agreement with the DNS results (Orlandi and Fatica, 1997) and experimental data (Reich and Beer, 1989). From Fig. 2(b), it is seen that the mean azimuthal velocity predicted by the present LES agrees well with the DNS results and experimental data. However, because the discrepancy between DSM results and experimental data is not small, it is somewhat difficult to show the validity of LDM compared with DSM in Fig. 2(b). Fig. 2(c) and (d) depicts the resolved axial turbulence intensity normalized by the pipe centerline velocity U_C and the resolved turbulent Reynolds stress $\langle v_r' v_z' \rangle$ normalized by the wall friction velocity of the pipe flow at $N = 0$, 1 and 2. The turbulence intensity and Reynolds stress are accurately calculated by the LES near the pipe wall and are in agreement with the DNS results. It is noted that the peak values of $v_{z\,\mathrm{rms}}'$ and $\langle v_r' v_z' \rangle$ near the wall predicted by DSM are somewhat larger than the results by LDM and the experimental data at $N = 1$. Other turbulence statistics predicted by the present LES, including the radial and azimuthal turbulence intensities and the other two cross Reynolds stresses, have also compared well with the DNS results (Orlandi and Fatica, 1997) and experimental data (Reich and Beer, 1989).

To validate the present calculation further, the turbulent flow in a concentric annular channel, corresponding to both the cases of $N = 0$ and 20 in the following section with the inner and outer cylinder radii being $R_o = 2$ and $R_i = 1$ as well as the annular channel length being $L_z = 15$, is calculated. Fig. 3(a) shows the distributions of the turbulence intensities at $N = 0$, $Re_\tau = 640$ (corresponding to $Re_m = 15{,}200$ approximately), where $y_d = (r - R_i)/(R_o - R_i)$. By comparing the present LES results with the experimental data at $Re_m = 13{,}300$ (Nouri et al., 1993), it is seen that the present LES results are in good agreement with the experimental data. Meanwhile, to demonstrate that the computed results are independent of the time steps and grid sizes, the turbulence intensities at $N = 20$, $Re_\tau = 640$ calculated by different grid numbers and time steps are shown in Fig. 3(b); both the results agree well each other.

Furthermore, the relevant computational code used in the present study has also been validated and verified by our previous work (Dong et al., 2003; Dong and Lu,

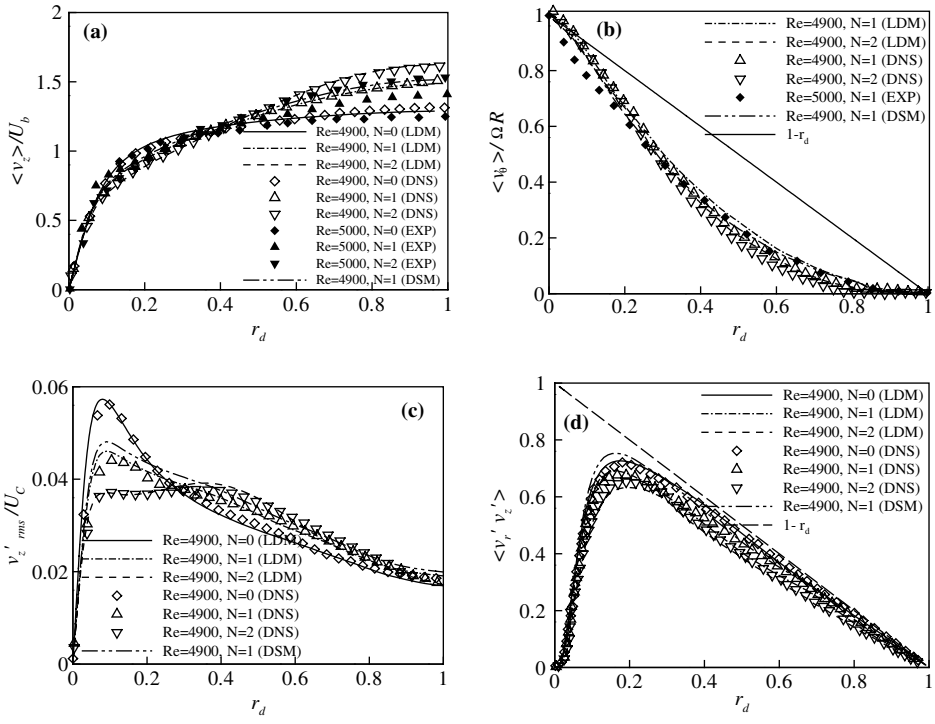

Fig. 2. Profiles of the mean axial and azimuthal velocity, axial turbulence intensity, and turbulent Reynolds stress $\langle v_r' v_z' \rangle$ of pipe flow and their comparisons with the DNS results and experimental data: (a) axial velocity; (b) azimuthal velocity; (c) axial turbulence intensity; (d) turbulent Reynolds stress $\langle v_r' v_z' \rangle$.

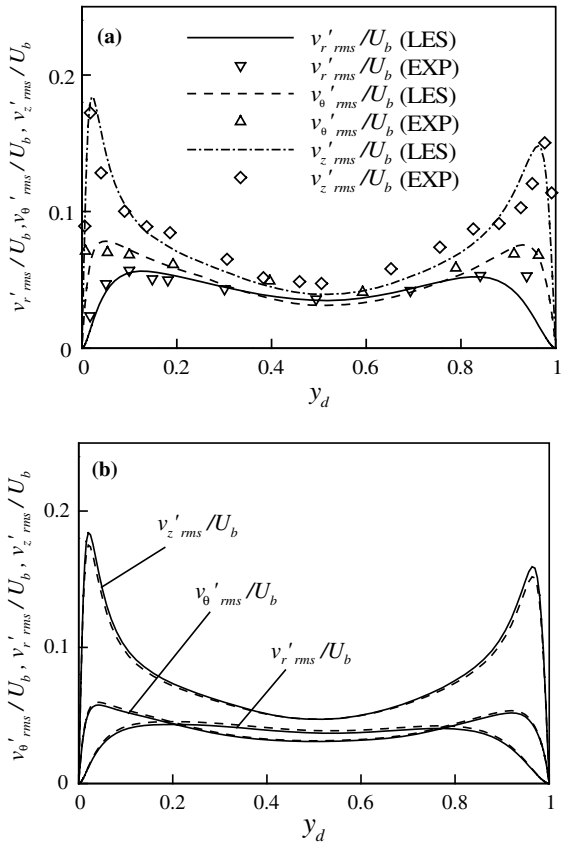

Fig. 3. Validations for turbulent annular channel flows: (a) turbulence intensities at $N = 0$,$Re_\tau = 640$ and their comparison with the experiment data; (b) Turbulence intensities at $N = 20$, $Re_\tau = 640$ calculated by grid number $97 \times 97 \times 128$ and time step 0.001 (solid lines) and by $129 \times 129 \times 192$ and time step 0.0005 (dashed lines).

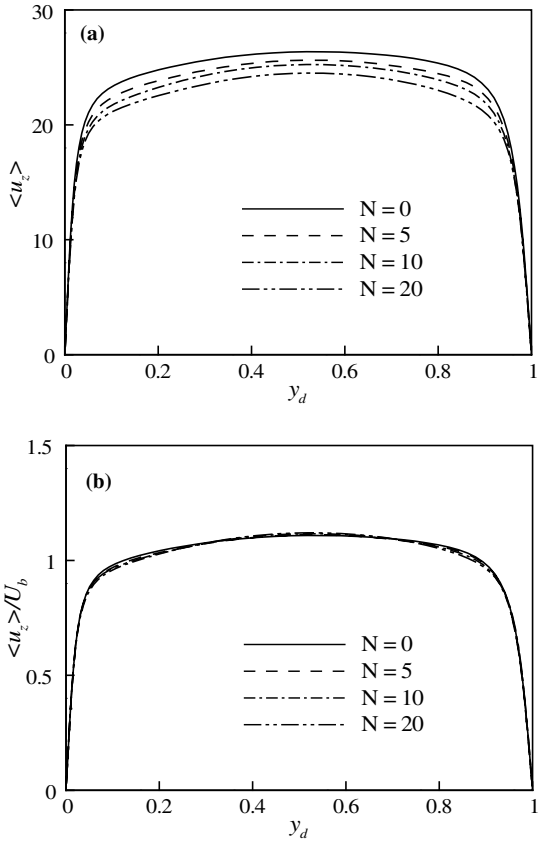

Fig. 4. Profiles of the mean axial velocity: (a) velocity normalized by the friction velocity u_τ, (b) velocity normalized by the bulk mean velocity U_b.

2004; Liu and Lu, 2004; Wang and Lu, 2004; Wang et al., 2005). Thus, it is confirmed that the present computational code is reliable to predict the turbulence characteristics in a rotating concentric annular channel.

4. Results and discussion

Turbulent flows in a rotating concentric annular channel are calculated for $Re_\tau = 640$ and $N = 0$–20. Based on the careful test calculations, e.g., as typically shown in Fig. 3, the inner and outer cylinder radii are set as $R_o = 2$ and $R_i = 1$, and the annular channel length is chosen as $L_z = 15$, which is a sufficient length to contain the largest coherent structure in the axial direction. Note that those length quantities are normalized by the gap width of the annular channel (i.e., $d = R_o - R_i$), as used in the non-dimensional governing equations early. Based on our validated calculations with different grid numbers and time steps, the grid system of $97 \times 97 \times 128$ in the radial, azimuthal and axial directions is adopted. The time step Δt is chosen as 0.001. As shown in Fig. 3(b), it has been verified that the present calculated results are independent of the grid number and time step. To achieve fine grid resolution near the walls, a stretching transformation is employed to cluster the grids near the inner and outer walls in the radial direction. The distance of the first grid point from the walls is $\Delta r^+ = 1$ approximately, while the maximum $\Delta r^+ = 15.4$ in the center of the channel, where the superscript "+" denotes the quantity normalized by the global friction velocity u_τ. Uniform mesh system is used in the azimuthal and axial directions with the grid increments $\Delta(R_i\theta)^+ = 42$ at the inner wall and $\Delta z^+ = 75$ respectively.

4.1. Mean velocity profiles

Profiles of the mean axial velocity are shown in Fig. 4. It is seen from Fig. 4a that the magnitude of axial velocity (or the corresponding bulk mean velocity U_b calculated based on the axial velocity profile) decreases with the increase of the rotation number due to the rotation effect. If the mean axial velocity is re-normalized by the bulk mean velocity U_b, as shown in Fig. 4(b), the distribution of the velocity only changes slightly in the central region of the annular channel for different rotation numbers. This behavior is similar to the streamwise

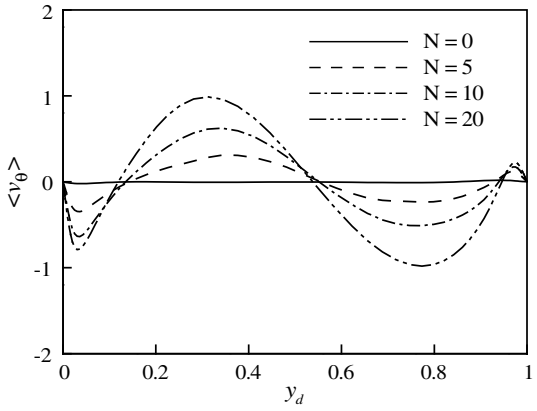

Fig. 5. Profiles of the mean azimuthal velocity.

rotating turbulent channel flow (El-Samni and Kasagi, 2001).

Fig. 5 shows the mean azimuthal velocity-induced by system rotation. In the non-rotating case, as expected, the mean azimuthal velocity is zero. While in the rotating cases, the non-zero mean azimuthal velocity in the rotating frame appears and becomes more notable as the rotation number increases. According to Speziale et al. (2000), the appearance of the non-zero azimuthal velocity indicates that there is a secondary flow in the annular channel, which shows a significant dependence on the rotation number. In the streamwise rotating turbulent planar channel flow, antisymmetric profiles of spanwise velocity about the planar channel centerline were observed and characterized by four zones with opposite spanwise motions (El-Samni and Kasagi, 2001). As shown in Fig. 5, it is noted that asymmetric profiles of the mean azimuthal velocity with four zones of opposite azimuthal motions are reasonably identified. Since the rotating axis is in accordance with the direction of mean flow for both the rotating turbulent flows mentioned above, it is reasonably predicted that the azimuthal motion in the axially rotating annular channel is qualitatively similar to the spanwise motion in the streamwise rotating planar channel. Furthermore, because the distinctive feature of the flow is the radial asymmetry of the velocity field for the annular channel flow, the zero locations of the profile have a tendency to become closer to the outer wall with respect to the streamwise rotating planar channel flow (El-Samni and Kasagi, 2001; Wu and Kasagi, 2004).

4.2. Turbulence intensities and Reynolds stresses

Fig. 6 shows the profiles of the root-mean-square (rms) values of the resolved velocity fluctuations (or the resolved turbulence intensities), normalized by the bulk mean velocity U_b, at different rotation numbers. Slight change of the axial turbulence intensity appears as the rotation number increases in Fig. 6(a). However,

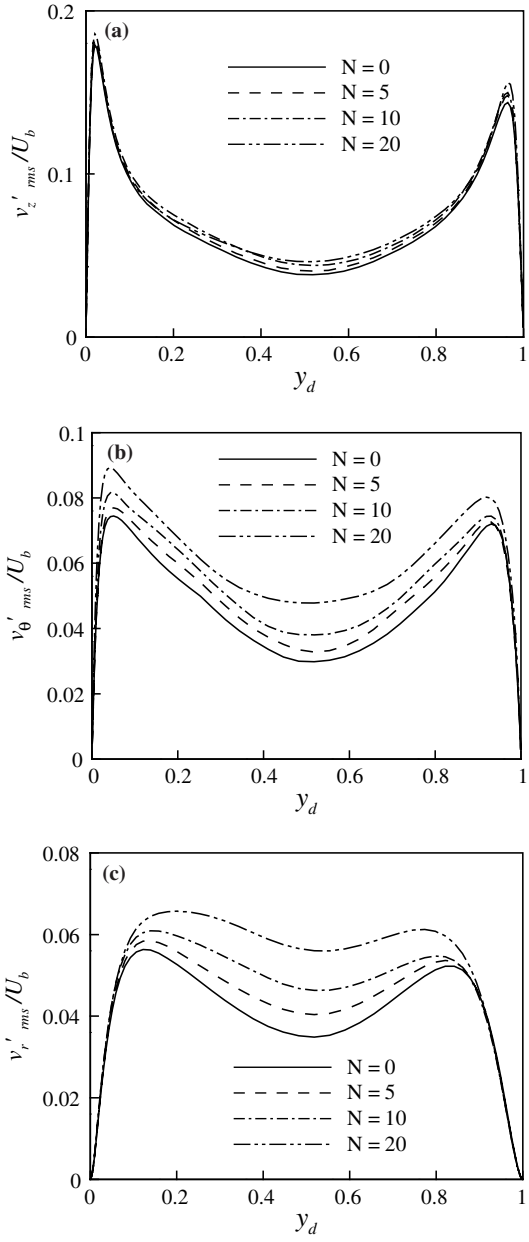

Fig. 6. Profiles of turbulent intensities: (a) axial; (b) azimuthal; (c) radial component.

as shown in Fig. 6(b) and (c), the radial and azimuthal turbulence intensities with remarkable peak values near the inner and outer walls are enhanced significantly in the central region of the annular channel in the rotating cases with the increase of the rotation number. This behavior is quite well consistent with the finding of the streamwise rotating planar channel flow (El-Samni and Kasagi, 2001). Since no Coriolis force term appears in the transport equation of $\langle v_z'^2 \rangle$, where v_z' represents the resolved axial velocity fluctuation, the variation of the turbulence intensities versus the rotation number can be attributed to the role that the pressure–strain correlation plays for turbulent energy redistribution (Moin and

Kim, 1982). The effect of system rotation modifies significantly the radial and azimuthal turbulence intensities, which is related to the interaction between the Coriolis force and velocity fluctuation based on the transport equations of $\langle v_\theta'^2 \rangle$ and $\langle v_r'^2 \rangle$, where v_θ' and v_r' denote the resolved azimuthal and radial velocity fluctuations, respectively. The intensification of the radial and azimuthal turbulence intensities in the central region of the rotating annular channel indicates that the turbulence there tends to be isotropic, especially at higher rotation number. This tendency was also observed in the rotating pipe flow (Orlandi and Fatica, 1997).

Fig. 7 shows the distributions of the resolved turbulent cross Reynolds stresses $\langle v_r' v_z' \rangle$ at several rotation numbers. It is seen from Fig. 7(a) that the profiles of $\langle v_r' v_z' \rangle$ change slightly for all the rotating cases. Since $\langle v_r' v_z' \rangle$ is mainly related to the production rate of the axial turbulent kinetic energy $\langle v_z'^2 \rangle$, as shown later, slight alteration of $\langle v_r' v_z' \rangle$ in the wall regions should be responsible for small modification of the axial turbulence intensity shown in Fig. 6(a).

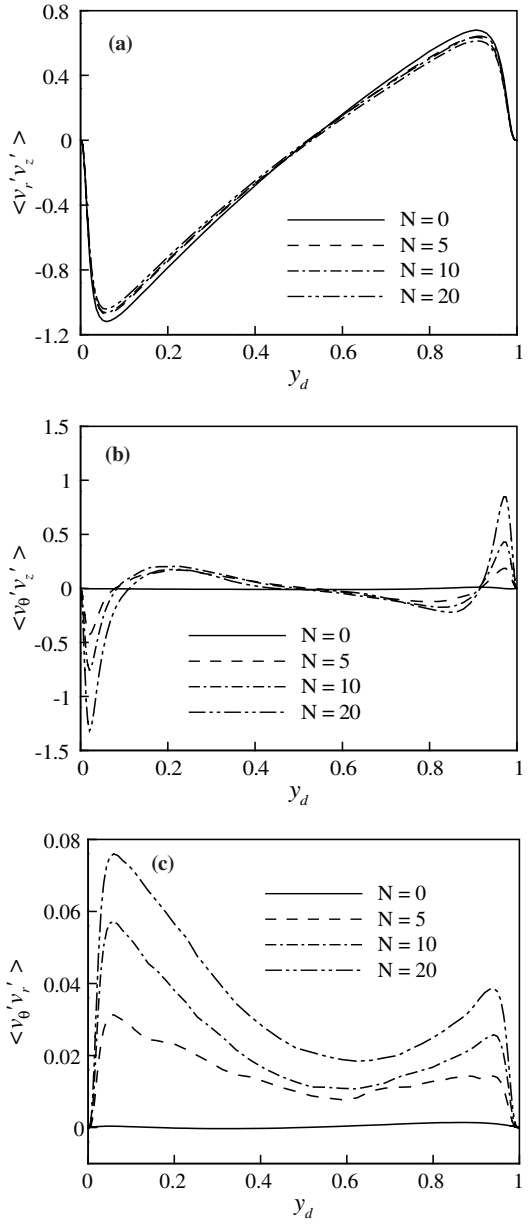

Fig. 7. Distributions of the resolved cross Reynolds stresses: (a) $\langle v_r' v_z' \rangle$; (b) $\langle v_\theta' v_z' \rangle$; (c) $\langle v_\theta' v_r' \rangle$.

As shown in Fig. 7(b) and (c), the rotation effect induces the non-zero Reynolds stresses, $\langle v_\theta' v_z' \rangle$ and $\langle v_\theta' v_r' \rangle$, which are augmented obviously near the inner and outer walls of the annular channel with the increase of the rotation number. In the rotating cases, $\langle v_\theta' v_z' \rangle$ becomes comparable to $\langle v_r' v_z' \rangle$ in the inner and outer wall regions, which is the result of the tilting of the near-wall vortical structures that strengthen the correlation between v_z' and v_θ' (Orlandi and Fatica, 1997). However, $\langle v_\theta' v_z' \rangle$ are small in the central region of the annular channel with respect to $\langle v_r' v_z' \rangle$. According to Orlandi and Fatica (1997), the profiles of $\langle v_\theta' v_r' \rangle$ in Fig. 7(c) indicates that the system rotation enhances the correlation between the radial velocity fluctuation v_r', which is generated by the near-wall turbulence events (i.e., ejection and sweep), and the azimuthal velocity fluctuation v_θ' in the wall regions. Thus, the larger value of $\langle v_\theta' v_r' \rangle$ near the inner wall with respect to that near the outer wall should be attributed to the more active turbulence events there.

4.3. High-order turbulence statistics

Figs. 8 and 9 exhibit the profiles of the skewness and flatness of the axial and radial velocity fluctuations near the inner and outer walls. Here, the distances from the inner wall and from the outer wall, i.e., y_i^+ and y_o^+, are defined as

$$y_\mathrm{i}^+ = (r - R_\mathrm{i}) u_\tau^\mathrm{i} / \nu \tag{18a}$$

$$y_\mathrm{o}^+ = (R_o - r) u_\tau^\mathrm{o} / \nu \tag{18b}$$

where u_τ^i and u_τ^o are the friction velocities at the inner and outer walls, respectively. The skewness factor S can be used to indicate whether positive or negative velocity fluctuation is dominant in the wall region. The fact that $S(u_\mathrm{i}') < 0$ indicates that the velocity fluctuation with $u_\mathrm{i}' < 0$ is dominant in probability; otherwise, the velocity fluctuation with $u_\mathrm{i}' > 0$ becomes dominant. While the flatness factor represents the intermittent character of wall turbulence.

As shown in Fig. 8(a) and (c), $S(v_z') > 0$ and $S(v_r') < 0$ near the inner wall indicate that the turbulence structures with $v_z' > 0$ and $v_r' < 0$, i.e., the high-speed elongated streaks, are attributed to scarce but strong sweep events in the inner wall region. Similar character is found in the outer wall region since $S(v_z') > 0$ and $S(v_r') > 0$ in Fig. 8(b) and (d). It is noticed that the skewness near the inner wall is higher than that near the outer wall, which should be owed to the appreciable change of

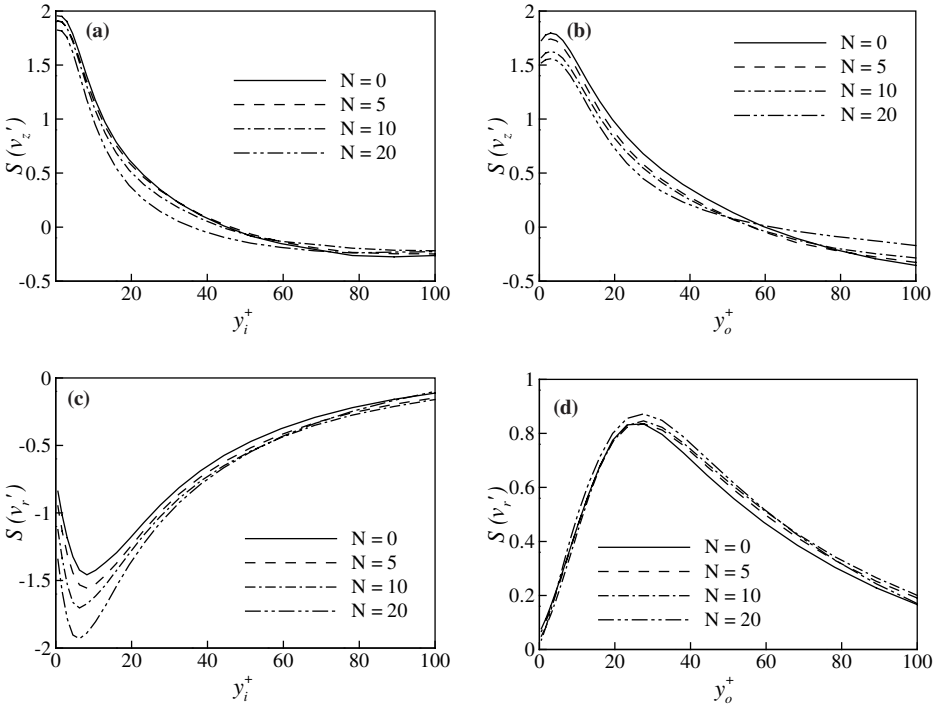

Fig. 8. Profiles of the skewness of the velocity fluctuations: (a) $S(v_z')$ near the inner wall; (b) $S(v_z')$ near the outer wall; (c) $S(v_r')$ near the inner wall; (d) $S(v_r')$ near the outer wall.

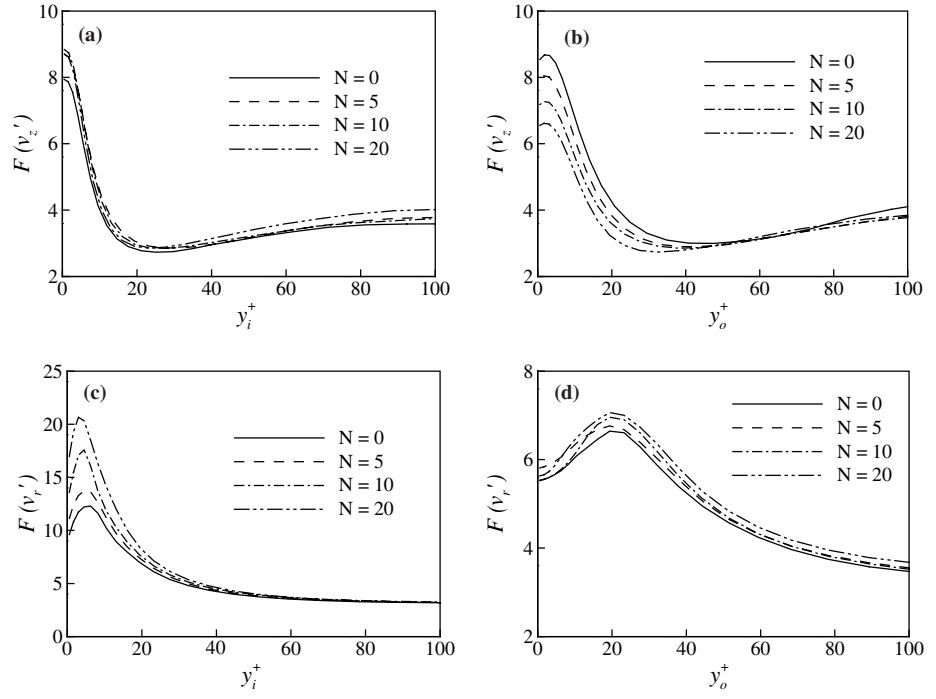

Fig. 9. Profiles of the flatness of the velocity fluctuations: (a) $F(v_z')$ near the inner wall; (b) $F(v_z')$ near the outer wall; (c) $F(v_r')$ near the inner wall; (d) $F(v_r')$ near the outer wall.

the orientation of the near-wall vortical structures, because the inclination of the vortical structures subject to system rotation is responsible to the modification of turbulence events and is relevant to the production of Reynolds stresses $\langle v_\theta' v_r' \rangle$ and $\langle v_\theta' v_z' \rangle$ in the wall region (Orlandi and Fatica, 1997). Based on the previous work for the plane channel flow (Kim et al., 1987) and pipe flow (Eggels et al., 1994), similar behavior has been found

that the flatness and skewness of the wall-normal (or radial) velocity fluctuations vary obviously. It is observed in Fig. 8(c) and (d) that the absolute peak values of $S(v_r')$ near the inner and outer walls increase with the increase of the rotation number.

Fig. 9 is the profiles of the flatness $F(v_z')$ and $F(v_r')$. As system rotation is imposed, $F(v_z')$ increases near the inner wall, which suggests that the axial turbulence fluctuation in the inner wall region becomes more intermittent in the rotating cases according to Orlandi and Fatica (1997). However, the reduction of $F(v_z')$ in the outer wall region indicates that the intermittence of the axial turbulence fluctuation decreases as the rotation number increases. As shown in Fig. 9(c) and (d), $F(v_r')$ near both the inner and outer walls are monotonously enhanced with the increase of the rotation number. This fact suggests that the radial turbulence fluctuations near the walls of the annular channel become more intermittent due to the rotation effect.

4.4. Turbulent stress budgets

The resolved Reynolds stress budgets provide detailed information of the dynamical characteristics of turbulence subjected to system rotation, e.g., turbulence energy production, dissipation and redistribution. Usually, the contribution of the axial Reynolds stress is important to the turbulent kinetic energy in this asymmetric turbulent flow, and the azimuthal turbulence fluctuation is modified significantly in the rotating annular channel. Thus, it is needed to investigate the turbulence production and dissipation rate in the wall regions based on the budgets of the axial and azimuthal normal Reynolds stresses, i.e., $\langle v_z'^2\rangle$ and $\langle v_\theta'^2\rangle$. On the other hand, the cross Reynolds stress $\langle v_\theta' v_z'\rangle$, which becomes comparable to $\langle v_r' v_z'\rangle$ in the wall regions in the rotating cases, exhibits a remarkable dependence on system rotation as shown in Fig. 7(b). The budget of $\langle v_\theta' v_z'\rangle$ is also of great help to deal with the mechanism of the rotation effect modifying $\langle v_\theta' v_z'\rangle$ in the rotating annular channel.

According to Moin and Kim (1982), the turbulence budgets of resolved Reynolds stresses in the rotating cylindrical coordinates are derived from the filtered Navier–Stokes equations by taking an ensemble average. Since turbulent annular flow is assumed fully developed and homogeneous in the azimuthal and axial directions, both the axial and azimuthal velocity components are non-zero. Thus, the remaining terms of the Reynolds stress budgets considered here are, according to the description of Moin and Kim (1982), turbulent diffusion (TDS), production rate (PRD), velocity pressure-gradient term (VPG), viscous diffusion rate (DFS), dissipation rate (DSP) and Coriolis force term (COR), and are presented as follows:

(1) Principal budget terms in the budget of $\langle v_z'^2\rangle$:

TDS (turbulent diffusion): $-\frac{1}{r}\left\langle\frac{\partial(r v_r' v_z'^2)}{\partial r}\right\rangle$;

PRD (production rate): $-2\langle v_r' v_z'\rangle\frac{\partial\langle\bar{v}_z\rangle}{\partial r}$;

VPG (velocity pressure-gradient term): $-2\left\langle v_z'\frac{\partial p'}{\partial z}\right\rangle$;

DFS (viscous diffusion rate): $\frac{1}{\mathrm{Re}_\tau}\left\langle\frac{1}{r}\frac{\partial}{\partial r}\left(r v_T\frac{\partial v_z'^2}{\partial r}\right)\right\rangle$;

DSP (dissipation rate): $-\frac{2}{Re_\tau}\left[\left\langle v_T\left(\frac{\partial v_z'}{\partial r}\right)^2\right\rangle + \frac{1}{r^2}\left\langle v_T\left(\frac{\partial v_z'}{\partial\theta}\right)^2\right\rangle + \left\langle v_T\left(\frac{\partial v_z'}{\partial z}\right)^2\right\rangle\right]$;

(2) Principal budget terms in the budget of $\langle v_\theta'^2\rangle$:

TDS (turbulent diffusion): $-\frac{1}{r^3}\left\langle\frac{\partial(r^3 v_r' v_\theta'^2)}{\partial r}\right\rangle$;

PRD (production rate): $-2\langle v_r' v_\theta'\rangle\frac{1}{r}\frac{\partial(r\langle\bar{v}_\theta\rangle)}{\partial r}$;

VPG (velocity pressure-gradient term): $-2\left\langle v_\theta'\frac{1}{r}\frac{\partial p'}{\partial\theta}\right\rangle$;

DSF (viscous diffusion rate): $\frac{1}{Re_\tau}\left\langle\frac{1}{r}\frac{\partial}{\partial r}\left[r^3 v_T\frac{\partial}{\partial r}\left(\frac{v_\theta'^2}{r^2}\right)\right]\right\rangle$;

DSP (dissipation rate): $-\frac{2}{Re_\tau}\left\{r^2\left\langle v_T\left[\frac{\partial}{\partial r}\left(\frac{v_\theta'}{r}\right)\right]^2\right\rangle + \frac{1}{r^2}\left\langle v_T\left(\frac{\partial v_\theta'}{\partial\theta}\right)^2\right\rangle + \left\langle v_T\left(\frac{\partial v_\theta'}{\partial z}\right)^2\right\rangle\right\}$;

COR (Coriolis force term): $-2N\langle v_\theta' v_r'\rangle$;

(3) Principal budget terms in the budget of $\langle v_\theta' v_z'\rangle$:

TDS (turbulent diffusion): $-\left\langle\frac{\partial(v_\theta' v_r' v_z')}{\partial r}\right\rangle$;

PRD (production rate): $-\left[\langle v_r' v_z'\rangle\frac{\partial\langle\bar{v}_\theta\rangle}{\partial r} + \langle v_r' v_\theta'\rangle\frac{\partial\langle\bar{v}_z\rangle}{\partial r}\right]$;

VPG (velocity pressure-gradient term): $-\left\langle v_\theta'\frac{\partial p'}{\partial z}\right\rangle$;

DFS (viscous diffusion rate): $\frac{1}{Re_\tau}\left\langle\frac{1}{r}\frac{\partial}{\partial r}\left(r v_T\frac{\partial v_\theta' v_z'}{\partial r}\right)\right\rangle$;

DSP (dissipation rate): $-\frac{2}{Re_\tau}\left[\left\langle v_T\frac{\partial v_\theta'}{\partial r}\frac{\partial v_z'}{\partial r}\right\rangle + \frac{1}{r^2}\left\langle v_T\frac{\partial v_\theta'}{\partial\theta}\frac{\partial v_z'}{\partial\theta}\right\rangle + \left\langle v_T\frac{\partial v_\theta'}{\partial z}\frac{\partial v_z'}{\partial z}\right\rangle\right]$;

COR (Coriolis force term): $-N\langle v_r' v_z'\rangle$;

where v_T represents the total relative viscosity, $v_T = 1 + v_\tau/v$.

Fig. 10(a), (b) and (c), (d) show the profiles of the terms in $\langle v_z'^2\rangle$ budget at $N = 0$ and 20, respectively. It is

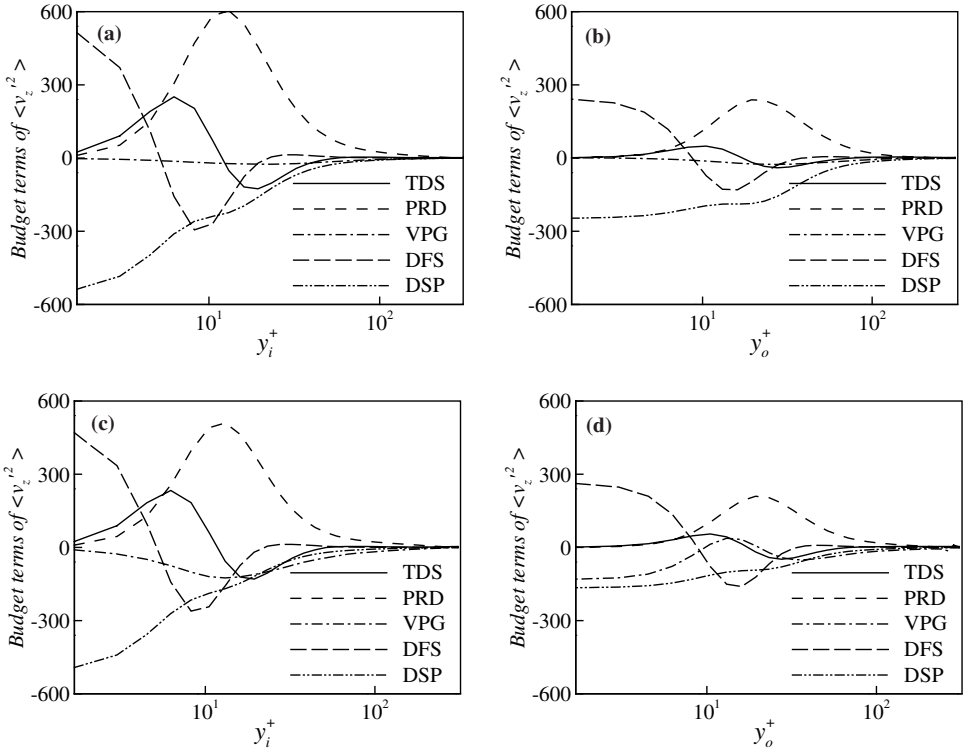

Fig. 10. Distributions of the budget terms in the transport equation of $\langle v_z'^2 \rangle$: (a) near the inner wall at $N = 0$; (b) near the outer wall at $N = 0$; (c) near the inner wall at $N = 20$; (d) near the outer wall at $N = 20$.

seen that the rotation effect suppresses the turbulence production rate of $\langle v_z'^2 \rangle$ evidently. The profile of PRD reaches the peak values about 600 and 236 near the inner and outer walls at $N = 0$, while 508 and 207 at

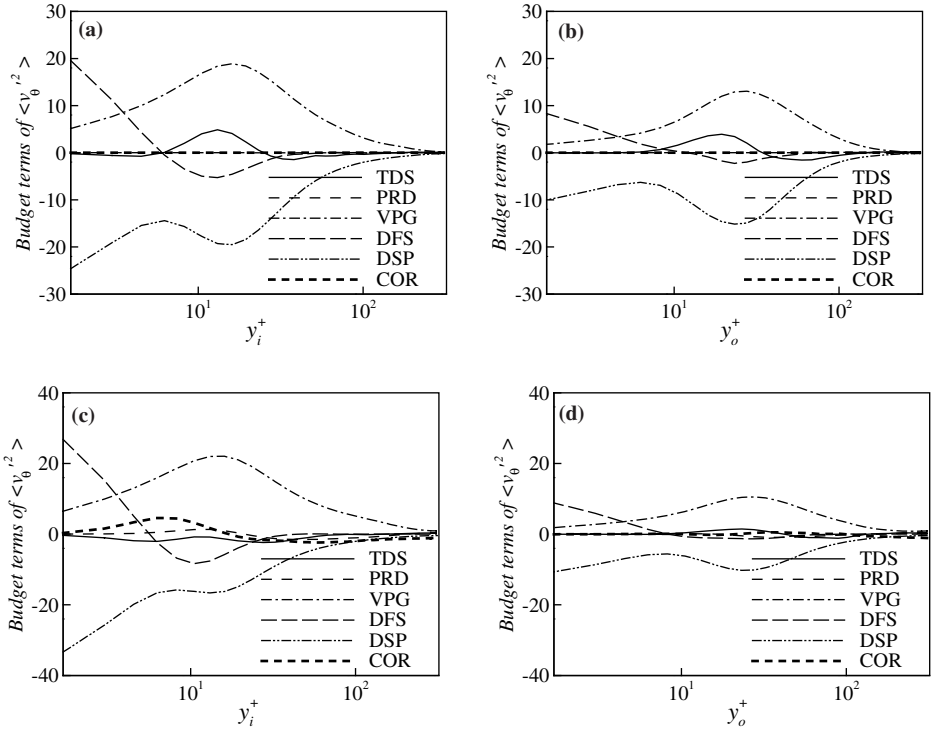

Fig. 11. Distributions of the budget terms in the transport equation of $\langle v_\theta'^2 \rangle$: (a) near the inner wall at $N = 0$; (b) near the outer wall at $N = 0$; (c) near the inner wall at $N = 20$; (d) near the outer wall at $N = 20$.

$N = 20$. It is found that the balance is achieved by the interaction between the viscous diffusion rate (DFS) and dissipation rate (DSP) in the wall regions for $N = 0$ and 20; while in the region $10 < y_i^+$(or y_o^+) < 100, the production rate plays main contribution to the $\langle v_z'^2 \rangle$ budget. In the central region of the annular channel, all the terms decay rapidly. In Fig. 10(c) and (d), the VPG term becomes comparable to the other terms. It is due to the fact that the centrifugal force in the rotating flow can be viewed as fictitious pressure which has been absorbed into the modified pressure. This feature results in that the VPG term plays an important role in the turbulence energy redistribution, which drains the turbulence energy from the axial turbulence fluctuation to the azimuthal and radial turbulence fluctuations. All the budget terms near the inner wall exhibit higher magnitudes compared to those near the outer wall, which is consistent with the profiles of the axial turbulence intensities near the walls, as shown in Fig. 6.

The profiles of $\langle v_\theta'^2 \rangle$ budget terms at $N = 0$ and 20 are plotted in Fig. 11(a), (b) and (c), (d), respectively. Even though system rotation induces non-zero azimuthal mean velocity in the annular channel, as shown in Fig. 5, the production rate in Fig. 11(c) and (d) still contributes little to the $\langle v_\theta'^2 \rangle$ budget at $N = 20$, compared to the DFS, VPG and DSP terms. All the terms in the $\langle v_\theta'^2 \rangle$ budget are smaller than those in the $\langle v_z'^2 \rangle$ budget. It is due to the fact that the azimuthal turbulence fluctuation is mainly generated by the sweep and ejection events related to the high- and low-speed elongated streaks in the walls regions, while the axial turbulence fluctuation is generated by the intensive mean flow shear. In both the non-rotating and rotating cases, the VPG term acts as a positive source term to the budget of $\langle v_\theta'^2 \rangle$. The contribution of the VPG term to $\langle v_\theta'^2 \rangle$ is mainly balanced by the DSP term in the region $8 < y_i^+$(or y_o^+) < 120. It is found that system rotation enhances the VPG term near the inner wall, while suppresses that near the outer wall. The Coriolis force term contributes little to the budget of $\langle v_\theta'^2 \rangle$ over the channel as shown in Fig. 11(c) and (d). This behavior is relevant to the distribution of $\langle v_\theta' v_r' \rangle$ that is the smallest one of the Reynolds stresses in the rotating cases, as shown in Fig. 7(c).

The budgets of cross Reynolds stress $\langle v_\theta' v_z' \rangle$ are shown in Fig. 12. At $N = 0$, the turbulent diffusion (TDS) and production rate (PRD) are the dominant terms to the $\langle v_\theta' v_z' \rangle$ budget. Since the rotation effect modifies significantly the near-wall distribution of $\langle v_\theta' v_z' \rangle$ by enhancing the correlation between v_z' and v_θ', all the terms of the $\langle v_\theta' v_z' \rangle$ budget shown in Fig. 12(c) and (d) are augmented remarkably in the rotating cases and are responsible to the balance of $\langle v_\theta' v_z' \rangle$ budget. The VPG term varies sharply near the walls with the peak values about -28 near the inner wall and 12 near the outer wall. Fig. 12(c) and (d) show that the Coriolis force term is also considerably contributed to the $\langle v_\theta' v_z' \rangle$ budget near the walls.

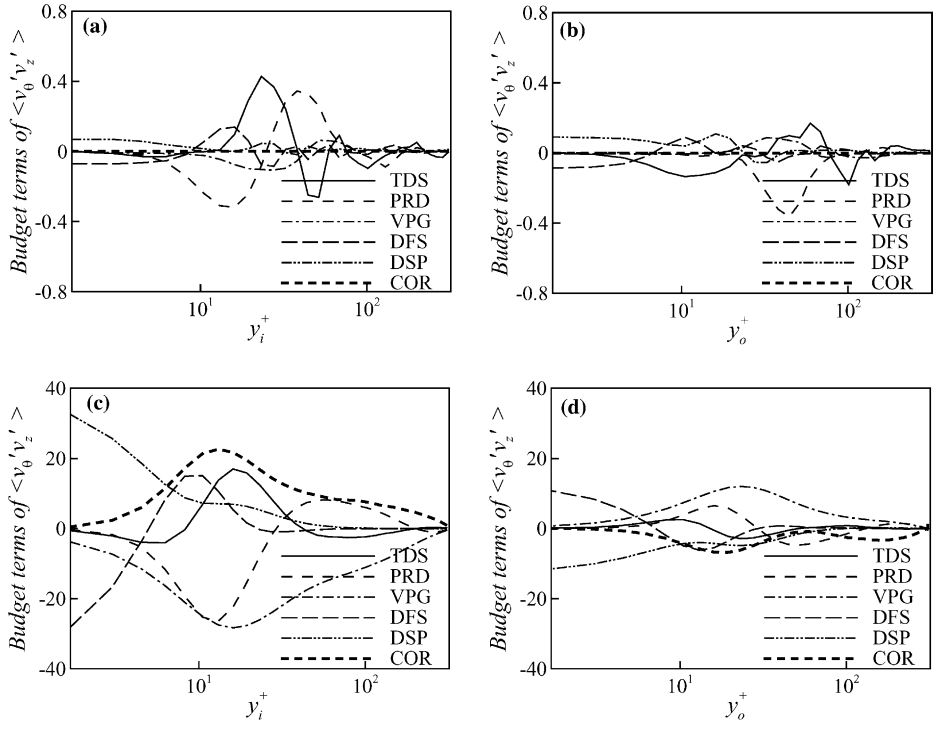

Fig. 12. Distributions of the budget terms in the transport equation of $\langle v_\theta' v_z' \rangle$: (a) near the inner wall at $N = 0$; (b) near the outer wall at $N = 0$; (c) near the inner wall at $N = 20$; (d) near the outer wall at $N = 20$.

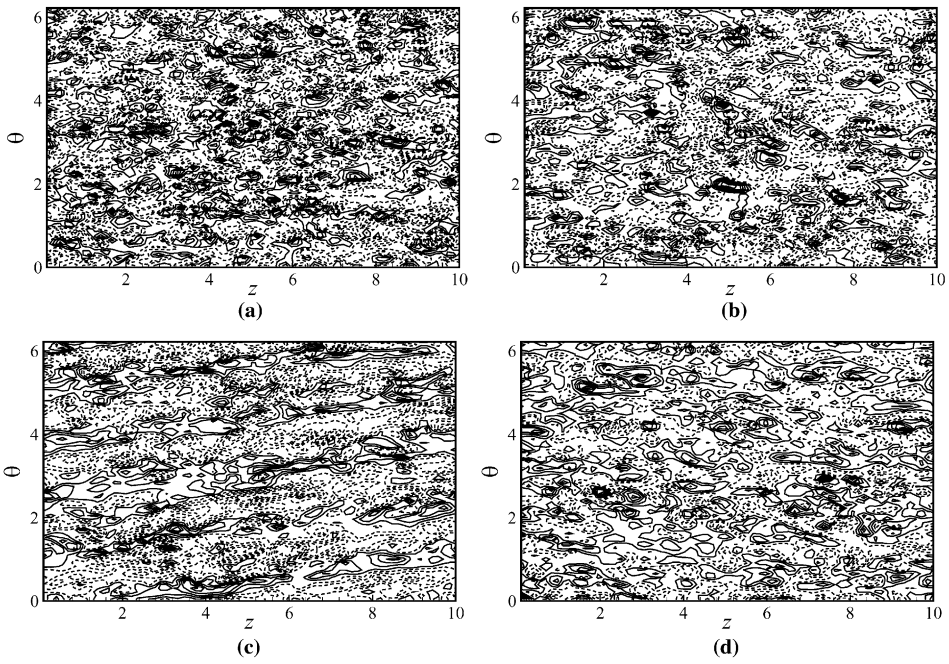

Fig. 13. Contours of instantaneous azimuthal velocity fluctuation in the (θ, z)-plane near the inner wall ($y_i^+ = 6.4$) and near the outer wall ($y_o^+ = 6.4$): (a) $y_i^+ = 6.4$, $N = 0$; (b) $y_o^+ = 6.4$, $N = 0$; (c) $y_i^+ = 6.4$, $N = 20$; (d) $y_o^+ = 6.4$, $N = 20$. Here, the increment of contour is 0.8.

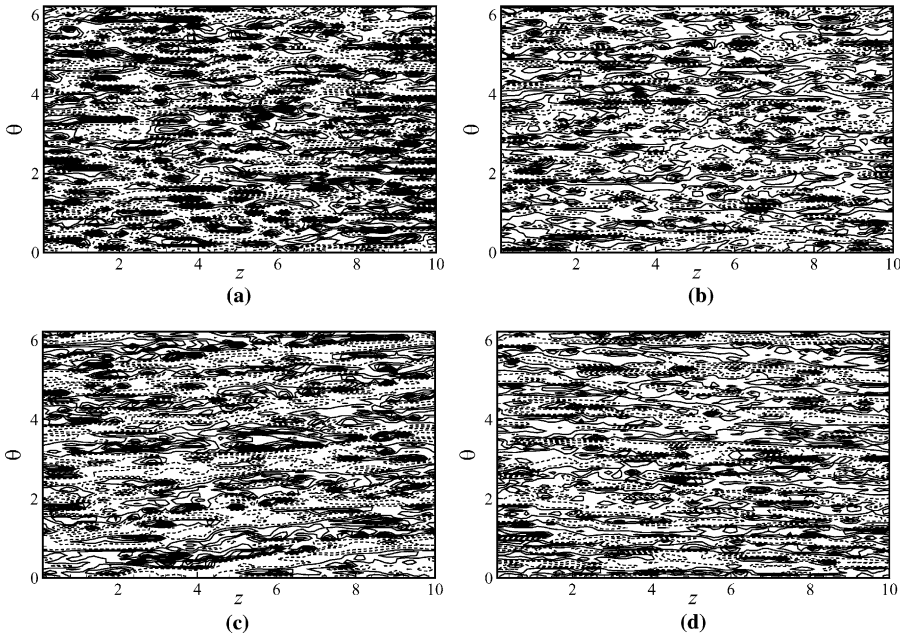

Fig. 14. Contours of instantaneous axial velocity fluctuation in the (θ, z)-plane near the inner wall ($y_i^+ = 6.4$) and near the outer wall ($y_o^+ = 6.4$): (a) $y_i^+ = 6.4$, $N = 0$; (b) $y_o^+ = 6.4$, $N = 0$; (c) $y_i^+ = 6.4$, $N = 20$; (c) $y_o^+ = 6.4$, $N = 20$. Here, the increment of contour is 3.

4.5. Flow structures

Contours of the instantaneous azimuthal and axial velocity fluctuations are of great help in revealing the influence of the rotation effect on turbulence coherent structures in the wall regions. Figs. 13 and 14 show the contours of the instantaneous azimuthal and axial velocity fluctuations in the (θ, z)-plane at $y_i^+ = 6.4$ (i.e., near the inner wall) and $y_o^+ = 6.4$ (i.e., near the outer wall) at $N = 0$ and 20, respectively. The patterns clearly illustrate the evolution of turbulent intensities with dense streaky structures near the inner wall in Figs. 13(c) and 14(c), compared to the streaky structures near

the outer wall in Figs. 13(d) and 14(d), which is consistent with the turbulence intensity distributions in Fig. 6.

Compared to the flow structures of the non-rotating case in Figs. 13(a), (b) and 14(a), (b), the scale of the streaky structures in the axial direction increases with the increase of the rotation number. It means that the rotation effect increases the scale of the vortical structures in the axial direction, which corresponds to a shift of turbulence energy distribution towards low wave number in spectral space. The transfer of turbulence energy from large scales to small ones is reduced due to the Coriolis force (Tritton, 1992). As shown in Fig. 5, the mean azimuthal velocity is negative near the inner wall and positive near the outer wall. Thus, as expected, it is seen that the upward inclination of the streaky structures appears near the inner wall in Fig. 13(c) and the downward inclination near the outer wall in Fig. 13(d). The inclination of the vortical structures near the walls is closely relevant to the dynamical characteristics of turbulence in the near-wall regions (Orlandi and Fatica, 1997).

5. Concluding remarks

Turbulent flows in a rotating concentric annular channel are investigated numerically by means of LES technique coupled with a localized one-equation dynamic subgrid-scale model. The decisive validation of the present approach has been achieved by comparing our calculated results with available DNS and experimental data for turbulent flows in a rotating pipe and in a concentric annular channel. Based on the present calculated results, it is found that the bulk mean axial velocity decreases; a non-zero azimuthal velocity arises and its magnitude increases with the increase of the rotation number. The rotation effect exhibits slight influence on the axial turbulence intensity but has significant change on the radial and azimuthal turbulence intensities. As the rotation number increases, the radial and azimuthal turbulence intensities are enhanced in the central region of the annular channel, and their peak values near the inner and outer walls increase. Meanwhile, the variation of the resolved Reynolds stresses, $\langle v'_\theta v'_z \rangle$ and $\langle v'_\theta v'_r \rangle$, is appreciable due to the rotation effect. The peak magnitudes of $\langle v'_\theta v'_z \rangle$ become comparable to those of $\langle v'_r v'_z \rangle$ near the inner and outer walls; it can be explained as a result of the tilting of the near-wall vortical structures that enhance the correlation between v'_z and v'_θ. In the rotating annular channel, the turbulence near the inner wall becomes more intermittent compared to that near the outer wall. The budgets of Reynolds stresses are calculated to examine the turbulence production rate, velocity and pressure gradient term, turbulent diffusion, dissipation rate and Coriolis force term near the walls. The Coriolis force term contributes to the balance of the $\langle v'^2_\theta \rangle$ and $\langle v'_\theta v'_z \rangle$ budget and becomes more important with the increase of the rotation number. Flow patterns based on the instantaneous velocity fluctuations are investigated to exhibit the influence of the rotation effect on turbulence structures near the wall regions.

Acknowledgments

This work was supported by the National Natural Science Foundation of China (Nos. 90405007, 10302028, 10125210), the Hundred Talents Programme of the Chinese Academy of Sciences (CAS), and Specialized Research Fund for the Doctoral Program of Higher Education (No. 20020358013).

References

Azouz, I., Shirazi, S.A., 1998. Evaluation of several turbulence models for turbulent flow in concentric and eccentric annuli. ASME J. Energy Resour. Technol. 120, 268–275.

Brighton, J.A., 1963. The structure of fully-developed turbulence flow in annuli. Ph.D. Thesis, Purdue University.

Brighton, J.A., Jones, J.B., 1964. Fully-developed turbulent flow in annuli. J. Basic Eng. D 86, 835–844.

Chung, S.Y., Rhee, G.H., Sung, H.J., 2002. Direct numerical simulation of turbulent concentric annular pipe flow Part 1: flow field. Int. J. Heat Fluid Flow 23, 426–440.

Dong, Y.H., Lu, X.Y., 2004. Large eddy simulation of a thermally stratified turbulent channel flow with temperature oscillation on the wall. Int. J. Heat Mass Transfer 47, 2109–2122.

Dong, Y.H., Lu, X.Y., Zhuang, L.X., 2003. Large eddy simulation of turbulent channel flow with mass transfer at high-Schmidt numbers. Int. J. Heat Mass Transfer 46, 1529–1539.

Eggels, J.G.M., Unger, F., Weiss, M.H., Westerweel, J., Adrian, R.J., Friedrich, R., Nieuwstadt, F.T.M., 1994. Fully developed turbulent pipe flow: a comparison between direct numerical simulation and experiment. J. Fluid Mech. 268, 175–209.

El-Samni, O.A., Kasagi, N., 2001. The effects of system rotation with three orthogonal rotating axes on turbulent channel flow. In: Proc. the ASME 7th Int. Conf. Fluid Dynamics Propulsion, Egypt.

Escudier, M.P., Gouldson, I.W., Jones, D.M., 1995. Flow of shear-thinning fluids in a concentric annulus. Exp. Fluids 18, 225–238.

Germano, M., Piomelli, U., Moin, P., Cabot, W.H., 1991. A dynamic subgrid-scale eddy viscosity model. Phys. Fluids A 3, 1760–1765.

Hanjalic, K., 1974. Prediction of turbulent flow in annular ducts with differential transport model of turbulence. Warme stoffubertragung. 7, 72–78.

Hasan, A., Roy, R.P., Kalra, S.P., 1992. Velocity and temperature fields in turbulent liquid flow through a vertical concentric annular channel. Int. J. Heat Mass Transfer 35, 1455–1467.

Heikal, M.R.F., Walklate, P.J., Hatton, A.P., 1976. The effect of free stream turbulence level on the flow and heat transfer in the entrance region of an annulus. Int. J. Heat Mass Transfer 20, 763–771.

Johnston, J.P., Halleen, R.M., Lezius, D.K., 1972. Effects of spanwise rotation on the structure of two-dimensional fully developed turbulent channel flow. J. Fluid Mech. 56, 533–557.

Kang, S., Patil, B., Zarate, J.A., Roy, R.P., 2001. Isothermal and heated turbulent upflow in a vertical annular channel—Part I.

Experimental measurements. Int. J. Heat Mass Transfer 44, 1171–1184.

Kim, W.W., Menon, S., 1997. Application of the localized dynamic subgrid-scale model to turbulent wall-bounded flows, AIAA paper 97-0210.

Kim, W.W., Menon, S., 1999. An unsteady incompressible Navier–Stokes solver for large eddy simulation of turbulent flows. Int. J. Numer. Methods Fluids 31, 983–1017.

Kim, J., Moin, P., Moser, R., 1987. Turbulence statistics in fully developed channel flow at low Reynolds number. J. Fluid Mech. 177, 133–166.

Kristoffersen, R., Andersson, H.I., 1993. Direct simulations of low-Reynolds-number turbulent flow in a rotating channel. J. Fluid Mech. 256, 163–197.

Lilly, D.K., 1992. A proposed modification of the Germano subgrid-scale closure method. Phys. Fluids A 4, 633–635.

Liu, N.S., Lu, X.Y., 2004. Large eddy simulation of turbulent concentric annular channel flows. Int. J. Numer. Methods Fluids 45, 1317–1338.

Liu, S.W., Meneveau, C., Katz, J., 1994. On the properties of similarity subgrid-scale models as deduced from measurements in a turbulent jet. J. Fluid Mech. 275, 83–119.

Malik, M.J., Pletcher, R.H., 1981. A study of some turbulence models for flow and heat transfer in ducts of annular cross-section. ASME J. Heat Transfer 103, 146–152.

Menon, S., Yeung, P.K., Kim, W.W., 1996. Effect of subgrid models on the computed interscale energy transfer in isotropic turbulence. Comput. Fluids 25, 165–180.

Moin, P., Kim, J., 1982. Numerical investigation of turbulent channel flow. J. Fluid Mech. 118, 341–377.

Nouri, J.M., Umur, H., Whitelaw, J.H., 1993. Flow of Newtonian and non-Newtonian fluids in concentric and eccentric annuli. J. Fluid Mech. 253, 617–641.

Orlandi, P., Fatica, M., 1997. Direct simulation of turbulent flow in a pipe rotating about its axis. J. Fluid Mech. 343, 43–72.

Pallares, J., Davidson, L., 2000. Large-eddy simulation of turbulent flow in a rotating square duct. Phys. Fluids 12, 2878–2893.

Piomelli, U., 1993. High Reynolds number calculations using the dynamic subgrid-scale stress model. Phys. Fluids A 5, 1484–1490.

Rai, M.M., Moin, P., 1991. Direct simulation of turbulent flow using finite-difference schemes. J. Comput. Phys. 96, 15–53.

Rehme, K., 1975. Turbulence measurements in smooth concentric annuli with small radius ratios. J. Fluid Mech. 72, 189–206.

Reich, G., Beer, H., 1989. Fluid flow and heat transfer in an axially rotating pipe—I. Effect of rotation on turbulent pipe flow. Int. J. Heat Mass Transfer. 32, 551–561.

Schumann, U., 1975. Subgrid scale model for finite difference simulations of turbulent flows in plane channels and annuli. J. Comput. Phys. 18, 376–404.

Schumann, U., 1977. Realizability of Reynolds-stress turbulence models. Phys. Fluids 20, 721–725.

Smagorinsky, J., 1963. General circulation experiments with the primitive equations. Mon. Weather Rev. 91, 99–112.

Speziale, C.G., Younis, B.A., Berger, S.A., 2000. Analysis and modeling of turbulent flow in an axially rotating pipe. J. Fluid Mech. 407, 1–26.

Tritton, D.J., 1992. Stabilization and destabilization of turbulent shear flow in a rotating fluid. J. Fluid Mech. 241, 503–523.

Velidandla, V., Putta, S., Roy, R.P., 1996. Turbulent velocity field in isothermal and heated liquid flow through a vertical annular channel. Int. J. Heat Mass Transfer 39, 3333–3346.

Verzicco, R., Orlandi, P., 1996. A finite-difference scheme for three-dimensional incompressible flows in cylindrical coordinates. J. Comput. Phys. 123, 402–413.

Wang, L., Dong, Y.H., Lu, X.Y., 2005. An investigation of turbulent open channel flow with heat transfer by large eddy simulation. Comput. Fluids 34, 23–47.

Wang, L., Lu, X.Y., 2004. An investigation of turbulent oscillatory heat transfer in channel flows by large eddy simulation. Int. J. Heat Mass Transfer 47, 2161–2172.

Wu, H.B., Kasagi, N., 2004. Effects of arbitrary directional system rotation on turbulent channel flow. Phys. Fluids 16, 979–990.

Yoshizawa, A., Horiuti, K., 1985. A statistically-derived subgrid-scale kinetic energy model for the large eddy simulation of turbulent flows. J. Phys. Soc. Jpn. 54, 2834–2839.

Zarate, J.A., Roy, R.P., Laporta, A., 2001. Isothermal and heated turbulent upflow in a vertical annular channel—Part II. Numerical simulations. Int. J. Heat Mass Transfer 44, 1185–1199.

Zang, Y., Street, R.L., Koseff, J.R., 1993. A dynamic mixed subgrid-scale model and its application to turbulent recirculating flows. Phys. Fluids A 5, 3186–3196.